

Corrosion Behavior of As-Cladding $\text{Al}_{0.8}\text{CrFeCoNiCu}_{0.5}\text{Si}_x$ High Entropy Alloys in 3.5% NaCl Solution

Yanzhou Li^{a,b} , Yan Shi^{c,d*}, Hua Lin^{a,b}, Xiaohu Ji^{a,b}

^aWest Anhui University, School of Mechanical and Vehicle Engineering, Yueliangdao Road, No. 1, 237010, Lu'an, China.

^bWest Anhui University, Innovation Platform of High-performance Complex Manufacturing Intelligent Decision and Control, 237012, Lu'an, China.

^cChangchun University of Science and Technology, School of Electromechanical Engineering, Weixing Road, No. 7089, 130022, Changchun, China.

^dNational Base of International Science and Technology Cooperation in Optics, Weixing Road, No. 7089, 130022, Changchun, China.

Received: May 03, 2023; Revised: November 22, 2023; Accepted: December 31, 2023

The corrosion behavior of $\text{Al}_{0.8}\text{CrFeCoNiCu}_{0.5}\text{Si}_x$ ($x=0, 0.2, 0.3$) high-entropy alloy laser cladding coatings in a 3.5% NaCl solution was investigated using polarization tests, impedance spectroscopy, scanning electron microscopy, and energy dispersive spectroscopy. As the Si content increased, the over-passivation potential and the width of the passivation zone for the $\text{Al}_{0.8}\text{CrFeCoNiCu}_{0.5}\text{Si}_x$ coating expanded, while the corrosion current density tended to decrease, enhancing the stability of the passivation film and the corrosion resistance of the coating. The $\text{Al}_{0.8}\text{CrFeCoNiCu}_{0.5}$ coating underwent selective corrosion, with some pitting corrosion distribution showing no apparent regularity. The $\text{Al}_{0.8}\text{CrFeCoNiCu}_{0.5}\text{Si}_{0.2}$ coating exhibited a distinct grain profile with a tendency towards intergranular corrosion. The aggregation of Cu-rich and Al-Ni intergranular phases in the eutectic structure led to preferential erosion at the grain boundaries by corrosion ions in the $\text{Al}_{0.8}\text{CrFeCoNiCu}_{0.5}\text{Si}_{0.2}$ coating. The $\text{Al}_{0.8}\text{CrFeCoNiCu}_{0.5}\text{Si}_{0.3}$ coating presented corrosion pits, although their distribution did not display apparent regularity. The $\text{Al}_{0.8}\text{CrFeCoNiCu}_{0.5}\text{Si}_x$ high-entropy alloy coating demonstrates superior corrosion resistance in solution compared to 5083 aluminum alloy.

Keywords: High entropy alloy, Laser cladding, Corrosion resistance, Corrosion behavior.

1. Introduction

Laser cladding, as an efficient and environmentally friendly technology, has been widely applied in material surface modification due to its advantages, such as low dilution rate, rapid cooling, and minimal thermal deformation^{1,2}. High-entropy alloys (HEAs) are a new type of alloy material, first proposed by Yeh et al.³ in 2004, defined as alloy systems composed of 5 to 13 elements in equiatomic or near-equiatomic ratios. Compared with traditional alloys, high-entropy alloys exhibit a high-entropy effect, sluggish diffusion effect, and lattice distortion effect, which can suppress the formation of ordered intermetallic compounds during the solidification process, favoring the formation of simple solid-solution structures. By reasonably adjusting the element ratios, high-entropy alloys can demonstrate excellent properties such as high hardness⁴, high strength⁵, corrosion resistance⁶, and outstanding wear resistance. Therefore, high-entropy alloys hold great potential for application in laser cladding materials.

The Al-Cr-Fe-Co-Ni-Cu system is a typical example of transition group HEAs. Scholars have studied its structure and properties. Tong et al.⁷ prepared AlCoCrCuFeNi

($x = 0 \sim 3.0$) HEAs using the arc melting method, and the alloys exhibited a simple fcc/bcc structure. With lower aluminum content, the alloy has a single fcc solid-solution structure. When $x = 0.8$, the alloy shows a composite structure of fcc eutectic phase and bcc eutectic. When $x > 1.0$, the alloy undergoes Spinodal decomposition, forming a modulated lamellar structure. When $x > 2.8$, a single-phase ordered bcc structure is obtained, the high mixing entropy and slow synergistic diffusion can promote the formation of simple phases and sub-micron and nanoscale precipitates in the alloy. Zhou et al.⁸ found that as-cast $\text{Al}_{0.4}\text{CoCrCuFeNi}$ HEA exhibits FCC1 phase and FCC2 phase, and it has sound antibacterial effects in the biocorrosion environment containing gram-negative *Pseudomonas aeruginosa* and gram-positive *Bacillus subtilis*. At the same time, its mechanical properties are better than 304 stainless steel. Chen et al.⁹ discovered that increased Cu content reduces the corrosion resistance and passivation film protection, but passivation treatment in 30wt% HNO₃ and 1wt% NaOH can increase the Cr³⁺ range in the passivation film of $\text{Al}_{0.3}\text{Cu}_x\text{CoCrFeNi}$ HEA, reducing the pitting tendency. However, excessive Cu content promotes the competition between the alloy containing Al and the Cu-rich phase, weakening the passivation treatment

*e-mail: lasercust@hotmail.com

effect, destroying the uniformity of the passivation film, and leading to severe galvanic corrosion.

In addition to changing the content of metallic elements in the alloy system, there are relevant studies on the structure and properties of alloys by adding non-metallic elements. Zhu et al.¹⁰ varied the content of Si in AlCoCrFeNi alloy and investigated its structure and properties. The results show that the AlCoCrFeNiSi_x alloy system mainly comprises BCC solid solutions, with silicon replacing other elements in the solid solution. The improvement of mechanical properties can be attributed to the solid-solution strengthening of silicon and the precipitation strengthening of nano-celled structures. Zhu et al.¹¹ analyzed that Si promotes the grain refinement strengthening of FeCoCrNiSi_x HEAs, with coating wear rates of 0.19 and $0.677 \times 10^{-4} \text{ mm}^3/\text{N} \cdot \text{m}$, significantly improving the wear resistance of the coating. The tribological properties of HEA coatings were studied at room temperature and 600°C when rubbed against Si3N4 balls, showing good wear resistance and anti-friction performance. Our study¹² on laser cladding Al_{0.8}CrFeCoNiCu_{0.5}Si_x (X=0,1~0.5) HEA coatings on aluminum alloy surfaces found that the coatings exhibited simple FCC and BCC phase structures, and the increase of Si content would cause the coating hardness first to increase and then decrease. The eutectic structure in the Al_{0.8}CrFeCoNiCu_{0.5}Si_{0.3} coating can increase the hardness of coating.

The above research findings show that the Al-Cr-Fe-Co-Ni-Cu system HEA has excellent wear and corrosion resistance. Meanwhile, non-metallic elements can potentially strengthen the performance of HEA coatings. Furthermore, the as-cladding Al_{0.8}CrFeCoNiCu_{0.5}Si_x HEA has demonstrated feasibility in improving the mechanical properties of aluminum alloy surfaces. However, the influence of Si content on the corrosion resistance of Al_{0.8}CrFeCoNiCu_{0.5} HEA needs to be further clarified. In this study, Si atoms were doped in Al_{0.8}CrFeCoNiCu_{0.5} HEA, and the effects of different Si contents on the corrosion resistance of HEA were studied using polarization tests and impedance spectroscopy analysis.

2. Experimental Details

The substrate used in the laser cladding process is a 5083 aluminum alloy, dimensioned at 50×30×10 mm. Prior to cladding, its oxide film is mechanically removed. The alloy's composition and content details are provided in Table 1.

Al, Fe, Cr, Ni, Co, Cu, and Si powders are selected and produced through atomization or reduction. This ensures

a purity level of at least 99.5% and particle sizes between 200 and 325 mesh. The specific composition ratios can be seen in Table 2. The powders are thoroughly mixed and homogenized using a QM-QX planetary ball mill for dry grinding over 15 hours, the milling speed of 200 rpm. To ensure cladding layer quality, preheat the substrate to 200°C, using high-purity argon gas as shielding gas in coaxial powder feeding at 5 L/min. The laser cladding process utilizes a 1500 W laser power, a 2.5 mm spot diameter, a scanning speed of 5 mm/s, and a 3 g/min powder feeding speed. After the coating is completed, it is encased in insulating cotton and allowed to cool gradually to prevent crack formation.

The electrochemical test sample preparation method is as follows: prepare the sample into a 10 mm x 10 mm testing surface, then polish it step by step using SiC sandpaper (with a maximum grit of 2000). Subsequently, thoroughly clean it with deionized water and anhydrous ethanol, and seal it with epoxy resin before connecting it to the working electrode. Polarization curves and impedance spectra tests are conducted on the Zennium Pro electrochemical workstation.

The testing employs a three-electrode system, which includes a saturated calomel electrode (SCE) as the reference electrode, a platinum (Pt) electrode with an electrode area of 1000 mm² as the counter electrode, and the prepared sample as the working electrode (WE) with an electrode area of 100 mm². Before initiating the electrochemical tests, the sample is immersed in the testing solution for one hour to achieve a relatively stable surface state. This procedure is commonly adopted to minimize distortions and oscillations during testing. Throughout this stage, the open-circuit potential (OCP) curves are observed, ensuring no variation exceeds 5 mV per second.

Electrochemical Impedance Spectroscopy (EIS) experiments are conducted prior to the potentiodynamic polarization techniques. For the EIS measurements, a potential amplitude of 10 mV, peak-to-peak (AC signal), is applied in an open-circuit setting, with data points logged every ten points per decade. The frequency range for EIS testing extends from 100 mHz to 10 kHz. The ZView software is utilized to propose equivalent circuits and process the data, with the EIS data being fitted and analyzed across a frequency range of 100 mHz to 10 kHz.

In the potentiodynamic polarization measurements, a scan rate of 0.3 mV/s is employed. The initial potential set for the potentiodynamic polarization curve test is -1.5 V, while the final potential reaches 1.5 V. Although a 0.3 mV/s is adopted in this stage of the experimentations, it is remarkable

Table 1. Elemental composition and content of 5083 aluminum alloy for experiments.

Element	Si	Cu	Mg	Zn	Mn	Ti	Cr	Fe	Al
Wt/%	≤0.4	≤0.1	4.0~4.9	≤0.25	0.4~1	≤0.15	0.05~0.25	0~0.4	Bal.

Table 2. Nominal component of Al_{0.8}CrFeCoNiCu_{0.5}Si_x.

Alloy	Abbreviation	Al	Cr	Fe	Co	Ni	Cu	Si
Al _{0.8} CrFeCoNiCu _{0.5}	Si0	15.09	18.86	18.86	18.86	18.86	9.43	0
Al _{0.8} CrFeCoNiCuSi _{0.2}	Si0.2	14.54	18.18	18.18	18.18	18.18	9.09	3.63
Al _{0.8} CrFeCoNiCu _{0.5} Si _{0.3}	Si0.3	14.28	17.85	17.85	17.85	17.85	8.92	5.35

that this selection has no provided substantial distortions in the polarization curves obtained. In this sense, it is worth noted that potential scan rate has an important role in order to minimize the effects of distortion in Tafel slopes and corrosion current density analyses, as previously reported¹³⁻¹⁶.

3. Results and Discussion

3.1. Potentiodynamic polarization curve analysis

Figure 1 displays the polarization curves of $\text{Al}_{0.8}\text{CrFeCoNiCu}_{0.5}\text{Si}_x$ coatings in a 3.5% NaCl solution, while Figure 2 provides in-depth Tafel extrapolations for these coatings. All samples exhibit a passivation range, which

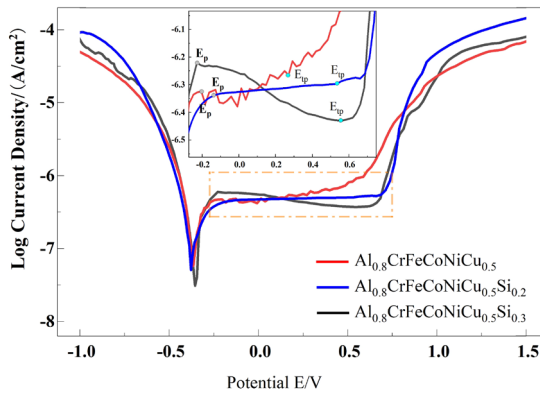


Figure 1. Polarization curves of $\text{Al}_{0.8}\text{CrFeCoNiCu}_{0.5}\text{Si}_x$ coatings.

means that during the electrochemical corrosion process, a passivation film is formed on the electrode surface, which helps to slow down the erosion of Cl ions on the working electrode surface. During anodic polarization, the passivation potential begins at the passivation potential (E_p). The passivation film ruptures when the trans passivation potential (E_{tp}) is exceeded in the polarization test. The width of the passivation range (ΔE) is the difference between the passivation potential and the trans passivation potential, which reflects the stability of the passivation film¹⁷. The passivation ranges of various HEA coatings are shown in the magnified view of Figure 1, with the passivation characteristic parameters listed in Table 3. As the Si content increases, E_{tp} and ΔE increase, indicating that adding Si elements makes the passivation film of the $\text{Al}_{0.8}\text{CrFeCoNiCu}_{0.5}\text{Si}_x$ HEA coating more stable. It is observed that the passivation range of Si0 presents a sawtooth shape, indicating that the passivation film formed during the polarization process does not entirely cover the sample surface, leading to localized corrosion in some areas.

The polarization curves were analyzed using the Tafel extrapolation method, as shown in Table 3. E_{corr} represents the corrosion potential, and i_{corr} represents the corrosion current density. The corrosion current densities for Si0 and Si0.2 are similar; however, Si0.3 exhibits a corrosion current density that is an order of magnitude lower than both Si0 and Si0.2. The addition of Si shows a decreasing trend in corrosion current density, indicating that Si helps to improve the corrosion resistance of the coating. SEM observations were carried out on the corroded coating surfaces further to analyze the corrosion mechanisms of the different component coatings.

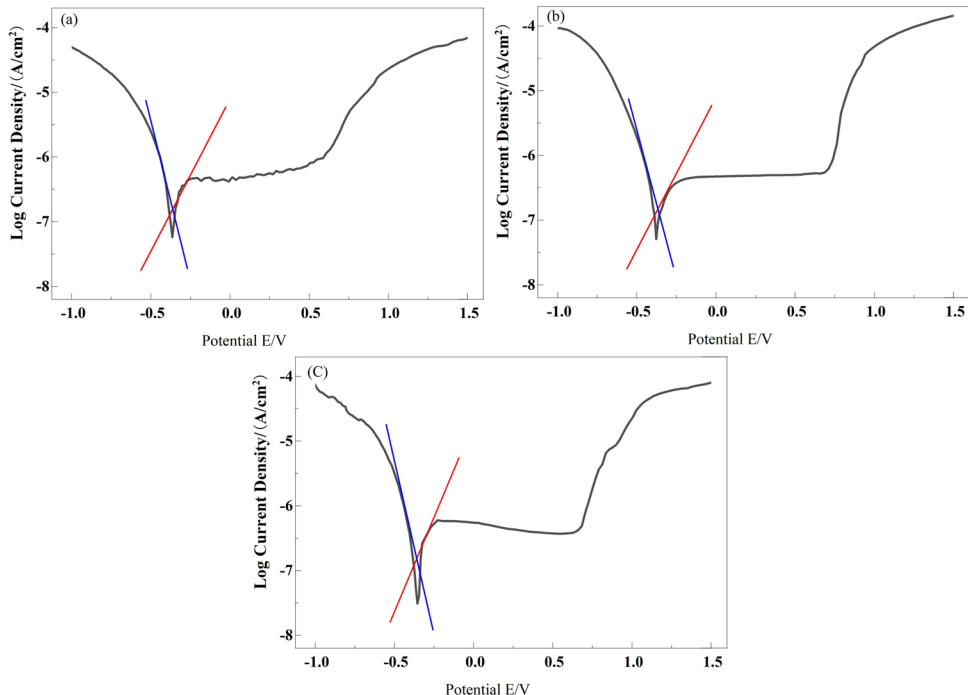


Figure 2. Detailed Tafel extrapolations of the polarization curves for $\text{Al}_{0.8}\text{CrFeCoNiCu}_{0.5}\text{Si}_x$ coatings from Figure 1. (a) $\text{Al}_{0.8}\text{CrFeCoNiCu}_{0.5}$; (b) $\text{Al}_{0.8}\text{CrFeCoNiCu}_{0.5}\text{Si}_{0.2}$; (c) $\text{Al}_{0.8}\text{CrFeCoNiCu}_{0.5}\text{Si}_{0.3}$.

3.2. Corrosion behavior of coatings and substrates

Figure 3 displays the corrosion morphology of the 5083 aluminum alloy and $\text{Al}_{0.8}\text{CrFeCoNiCu}_{0.5}\text{Si}_x$ coatings in a 3.5% NaCl solution. As evident in Figure 3a, the substrate has undergone extensive corrosion, whereas the HEA coating surfaces, shown in Figures 3b-d, remain relatively intact with visible corrosion products. Figure 3b reveals selective corrosion patterns on the Si0 coating, characterized by irregularly distributed pitting. These pits exhibit some traces of intergranular corrosion but do not appear to spread or expand significantly. In Figures 3c and 3d, the Si0.2 and Si0.3 coatings show clear grain boundaries, indicating a tendency towards intergranular corrosion, no pronounced intergranular corrosion is observed. The Si0.3 coating surface features corrosion pits without a clear distribution pattern. Energy-dispersive X-ray spectroscopy (EDS) analysis of the corrosion products from each coating indicates they primarily consist of copper oxides and chlorides. This suggests that the Cu-rich phase is the most susceptible to corrosion.

Figure 4 shows the corrosion mechanism diagram of the $\text{Al}_{0.8}\text{CrFeCoNiCu}_{0.5}\text{Si}_x$ system coating. Figure 4a and Figure 4b show the electrode particle distribution states in the electrolyte solution and the formation of the passivation film, respectively, before and during the polarization test. Our Early research showed that $\text{Al}_{0.8}\text{CrFeCoNiCu}_{0.5}\text{Si}_x$ coatings mainly comprise Cu-rich FCC1, BCC1, and BCC2 phases, without forming complex intermetallic compound structures. The FCC1 is Cu-rich and mainly exists in the intergranular structure. BCC1 is Fe-, Cr-rich, BCC2 is Al-, Ni-rich, and Si exists in the system as a solid solution. Due to the potential difference between grain boundaries and intergranular regions with different chemical compositions during the electrolyte solution corrosion process, the coating will experience galvanic corrosion effects during the electrochemical corrosion process¹⁸. The grain boundaries of the coating is enriched in Al, Ni, and Cu elements, and the grains are enriched in Fe and Cr elements. The dissolution process of the anode involves the metal entering the corrosive solution in the form of ions while the electrons remain in the metal matrix. In electrolyte solutions, Al, Cu, and Ni react with chloride

Table 3. The electrochemical parameters of $\text{Al}_{0.8}\text{CrFeCoNiCu}_{0.5}\text{Si}_x$ coating.

Samples	E_{corr}/V	$i_{\text{corr}}/(\mu\text{A}\cdot\text{cm}^{-2})$	E_p/V	E_{tp}/V	$\Delta E/\text{V}$
Si0	0.361(\pm 0.0045)	0.167(\pm 0.0085)	-0.181(\pm 0.0095)	0.270(\pm 0.004)	0.451(\pm 0.008)
Si0.2	-0.378(\pm 0.0092)	0.141(\pm 0.0017)	-0.157(\pm 0.0043)	0.538(\pm 0.011)	0.695(\pm 0.006)
Si0.3	-0.355(\pm 0.019)	0.087(\pm 0.0009)	-0.226(\pm 0.0046)	0.556(\pm 0.019)	0.782(\pm 0.009)

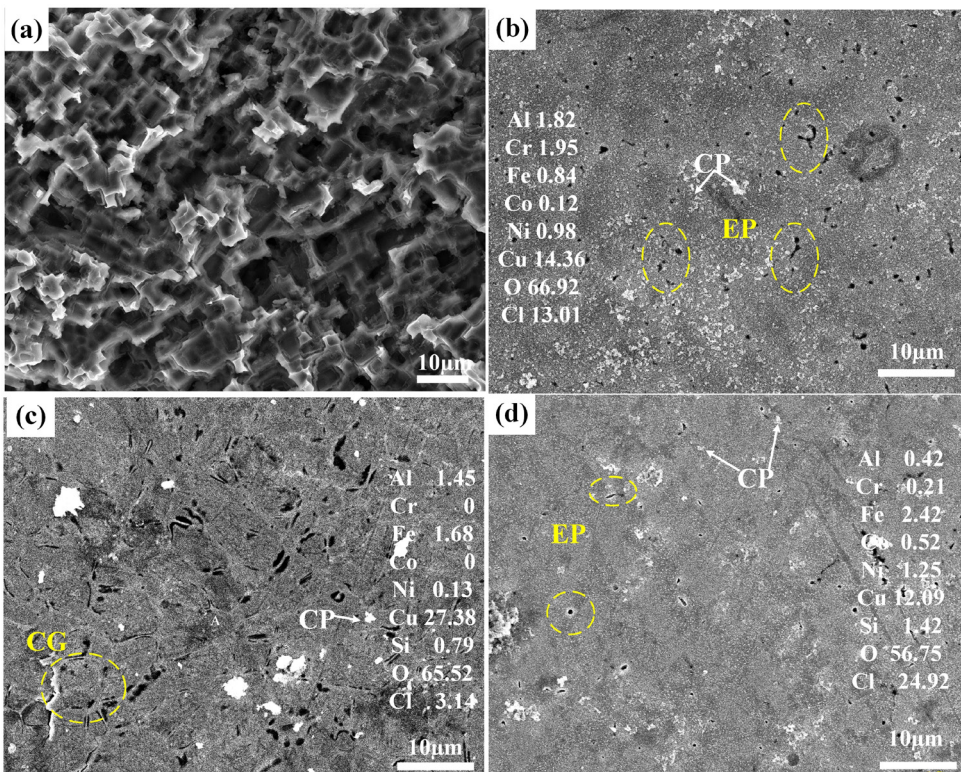


Figure 3. Corrosion morphology of the $\text{Al}_{0.8}\text{CrFeCoNiCu}_{0.5}\text{Si}_x$ coating and substrate. (a) Substrate; (b) $\text{Al}_{0.8}\text{CrFeCoNiCu}_{0.5}$; (c) $\text{Al}_{0.8}\text{CrFeCoNiCu}_{0.5}\text{Si}_{0.2}$; (d) $\text{Al}_{0.8}\text{CrFeCoNiCu}_{0.5}\text{Si}_{0.3}$.

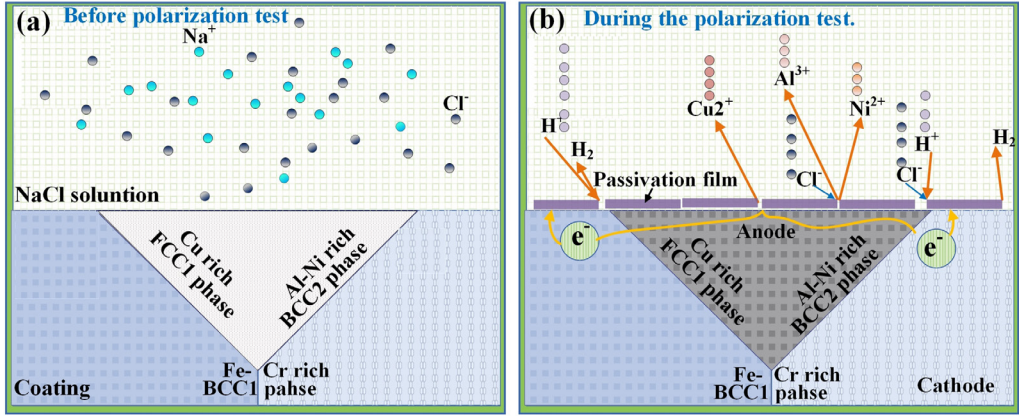
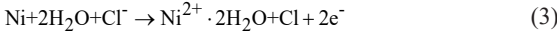
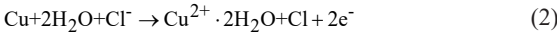
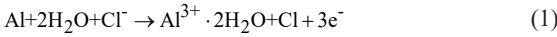


Figure 4. The corrosion mechanism diagram of $\text{Al}_{0.8}\text{CrFeCoNiCu}_{0.5}\text{Si}_x$ coatings. (a) Before polarization test (b) During the polarization test.

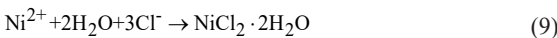
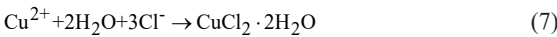
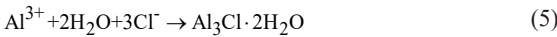
ions according to the reactions detailed in Equations 1, 2 and 3, respectively. The equation is as follows:



The dissolution process of the anode involves the metal entering the corrosive solution in the form of ions while the electrons remain in the metal matrix. The equation is as follows:



The dissolution process of the anode involves the metal entering the corrosive solution in the form of ions while the electrons remain in the metal matrix. The reactions for Al cations, Cu cations, and Ni cations in this process are represented by Equations 5 and 6 for Al, Equations 7 and 8 for Cu, and Equations 9 and 10 for Ni. The equation is as follows:



From the perspective of polarization passivation, the passivation film formed by the Cr-rich BCC1 phase

provides better protection, resulting in a complete corrosion morphology for the HEA coating than the substrate. At the same time, with the addition of Si, the microstructure of HEA coating evolves from a dendritic structure ($x=0$) to a dendritic structure with secondary dendrite arms ($x=0.2$) and finally to a eutectic structure ($x=0.3$)¹². Due to the presence of secondary dendrite arms in the Si0.2, the dendrite network formed by the FCC structure in the unit area is denser, making its polarization morphology exhibit the most significant intergranular corrosion characteristics. From the polarization curve test and corrosion analysis, Si0.3 has enhanced corrosion resistance compared to Si0.1. It is speculated that adding Si lowers Cu content. This decrease in Cu-rich phase content leads to an overall enhancement in the coating's corrosion resistance performance.

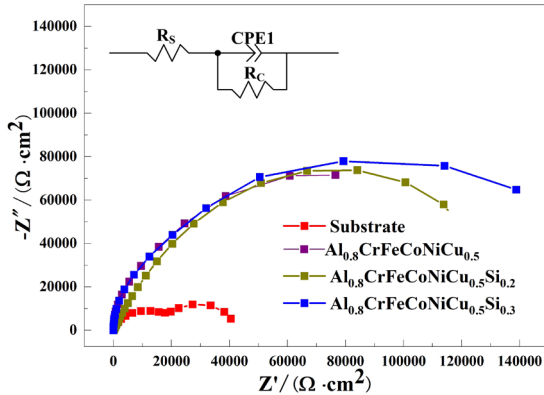
3.3. Impedance spectrum testing of coatings and substrates

Figure 5 presents the Nyquist plots for both the substrate and the coatings. The plots show that all coatings have single capacitive semicircles in the high-frequency range, which reveals that charge transfer occurs between the working electrode surface and the solution, forming a double-layer capacitance. The capacitive arc radius of HEA coatings is significantly larger than that of the substrate, indicating superior corrosion resistance compared to the substrate for the HEAs. Comparing the capacitive arc radii among the coatings, an increase in Si content results in a larger capacitive arc radius, suggesting that the passive film formed is more stable. This trend is in agreement with the polarization curve results.

Table 4 presents the equivalent circuit model of the coatings. The equivalent circuit consists of the solution resistance (R_s), charge transfer resistance (R_c), and the constant phase element CPE. Since an equivalent circuit is used in order to determine the simulated values and compare with experimental data, a CNLS (complex non-linear least squares) simulation is adopted in order to fitting the experimental and simulated data, as previously reported was carried out^{13,14,19-22}. The constant phase element formation occurs for the following reasons: During the electrochemical reaction process, the electrolyte solution causes metal ions

Table 4. Equivalent circuit parameters of HEA coatings.

	$R_s / (\Omega \cdot \text{cm}^2)$	CPE1		$R_c / (\text{k}\Omega \cdot \text{cm}^2)$
		$Y / (\mu\text{F} \cdot \text{cm}^2)$	n	
Si0	5.7(± 0.062)	29.9(± 0.507)	0.920	232.3(± 6.23)
Si0.2	2.2(± 0.015)	17.5(± 0.475)	0.916	225.9(± 8.954)
Si0.3	0.7(± 0.0094)	13.3(± 0.475)	0.931	317.3(± 20.63)

**Figure 5.** Nyquist plots of $\text{Al}_{0.8}\text{CrFeCoNiCu}_{0.5}\text{Si}_x$ coatings and substrate.

to leave the working electrode surface, leading to a negative potential as the metal loses positive ions. Metal ions in the solution are attracted to anions or electrons on the metal electrode surface and re-adsorb onto the metal surface. Anions (Cl^- , OH^-) in the electrolyte solution are attracted to cations on the metal surface, where they gather and form ionic precipitates through chemical reactions. When the solution's concentration reaches a specific value, the metal dissolution and ionic precipitation processes reach a dynamic equilibrium, including a double layer at the interface between the metal and the solution, which consists of a compact layer and a diffusion layer. Considering the non-uniform smoothness of the electrode surface, the electrode's double-layer capacitance and solid capacitance respond differently to the time response frequency during EIS testing. Using pure rather than double-layer capacitance can lead to a dispersion effect, resulting in a deviation of the impedance spectrum test results from the actual results. Therefore, the constant phase angle element CPE is used as a replacement for the equivalent circuit parameter element, with the impedance Z_{CPE} calculation expression as follows²³:

$$Z_{\text{CPE}} = Y_0^{-1} (j\omega)^{-n} = Y_0 \omega^{-n} \cos \frac{n\pi}{2} + j Y_0 \omega^n \sin \frac{n\pi}{2} \quad (11)$$

Y_0 is the proportionality factor, j is the imaginary unit, ω is the test current angular frequency, and n is the dispersion coefficient. The n represents the degree of dispersion of the equivalent circuit capacitance, the degree of uneven current distribution, with calculated results ranging from -1 to 1²⁴. When $4=1$, it represents an ideal capacitive circuit; when $4=0.7$, it represents a porous electrode circuit; when $n=0.5$, it represents Warburg diffusion impedance; when $4=0$, it

represents a purely resistive circuit; when $4=-1$, it means a strictly inductive circuit. The closer the value of 4 is to 1, the more uniform and compact the electrode surface; the further it deviates from 1, the more the porous structure affects the electrode surface.

Using Zview software to fit the impedance spectrum data, the results are shown in Table 4. The n values of Si0, Si0.2, and Si0.3 coatings are 0.920, 0.916, and 0.931, respectively, between 0.7 and 1, demonstrating that the coating surface is relatively uniform and dense and not susceptible to overall corrosion in a 3.5% NaCl solution. Before the addition of Si, the charge transfer resistance R_c is 232.3 $\text{k}\Omega \cdot \text{cm}$. After adding 0.3 Si, the charge transfer resistance R_c increases, indicating that the Si0.3 coating has a weaker charge transfer ability between the surface and the electrochemical corrosion medium.

4. Conclusions

1. Adding Si elements to the $\text{Al}_{0.8}\text{CrFeCoNiCu}_{0.5}\text{Si}_x$ coating can improve its passivation corrosion resistance in a 3.5% NaCl solution. With the increase of Si content, the transmissive potential (E_{tp}) and the width of the passivation region increase while the corrosion current density decreases. The corrosion resistance of the $\text{Al}_{0.8}\text{CrFeCoNiCu}_{0.5}\text{Si}_x$ HEA coating in the solution is better than that of the substrate.
2. The addition of Si causes the corrosion of the coating to affect the corrosion behavior and polarization morphology of the alloy. Si0.2 exhibits selective corrosion, with some pitting distributed irregularly. Si0.2 shows an intergranular corrosion tendency with distinct grain boundaries. The Si0.3 coating surface has corrosion pits, but the distribution pattern is not apparent.
3. During the EIS process, a double-layer structure forms between the sample, the metal surface, and the solution. The sample capacitive arc radius enlarges with increased Si content, while passivation film stability on the coating improves.

5. Acknowledgments

This study was supported by the High-level Talents Research Project of West Anhui University (Grant Nos. WGKQ2021068 and WGKQ2022058).

6. References

1. Yu PC, Liu XB, Lu XL, Qiao SJ, Zhai YJ, Zhu GX, et al. Tribology and high-temperature oxidation behaviors of NiCrBSiFe composite coatings on Ti6Al4V alloy by laser cladding. RSC Advances. 2015;5(93):76516-25.

- Li Y, Shi Y. Microhardness, wear resistance, and corrosion resistance of $\text{Al}_x\text{CrFeCoNiCu}$ high-entropy alloy coatings on aluminum by laser cladding. *Opt Laser Technol.* 2021;134:106632.
- Yeh JW, Chen SK, Lin SJ, Gan JY, Chin TS, Shun TT, et al. Nanostructured high-entropy alloys with multiple principal elements: novel alloy design concepts and outcomes. *Adv Eng Mater.* 2004;6(5):299-303.
- Mann AE, Newkirk JW. Compositional modifications to alter and suppress laves phases in $\text{Al}_x\text{CrMoTaYTi}$ Alloys. *Adv Eng Mater.* 2023;25(14):2201614.
- Yin BL, Curtin WA. Origin of high strength in the CoCrFeNiPd high-entropy alloy. *Mater Res Lett.* 2020;8(6):209-15.
- Wang Y, Zhao HY, Liu C, Ootani Y, Ozawa N, Kubo M. Mechanisms of chemical-reaction-induced tensile deformation of an Fe/Ni/Cr alloy revealed by reactive atomistic simulations. *RSC Advances.* 2023;13(10):6630-6.
- Tong CJ, Chen YL, Chen SK, Yeh JW, Shun TT, Tsau CH, et al. Microstructure characterization of $\text{Al}_x\text{CoCrCuFeNi}$ high-entropy alloy system with multiprincipal elements. *Metall Mater Trans, A Phys Metall Mater Sci.* 2005;36(4):881-93.
- Zhou EZ, Ren GY, Sun YL, Fan YQ, Yang Y, Sun MY, et al. Antibacterial activities of a novel Cu-bearing high-entropy alloy against multi-drug-resistant *Acinetobacter baumannii* and *Staphylococcus aureus*. *Rare Met.* 2022;41(2):570-9.
- Chen XD, Qian HC, Lou YT, Yang B, Cui TY, Zhang DW. Effects of Cu-content and passivation treatment on the corrosion resistance of $\text{Al}_{10.3}\text{Cu}_x\text{CoCrFeNi}$ high-entropy alloys. *J Alloys Compd.* 2022;920:165956.
- Zhu JM, Fu HM, Zhang HF, Wang AM, Li H, Hu ZQ. Synthesis and properties of multiprincipal component AlCoCrFeNiSix alloys. *Mater Sci Eng A.* 2010;527(27-28):7210-4.
- Zhu ZX, Liu XB, Liu YF, Zhang SY, Meng Y, Zhou HB, et al. Effects of Cu/Si on the microstructure and tribological properties of FeCoCrNi high entropy alloy coating by laser cladding. *Wear.* 2023;512-513:204533.
- Li YZ, Shi Y. Phase assemblage and wear resistance of laser-cladding $\text{Al}(0.8)\text{FeCoNiCrCu}(0.5)\text{Si}(x)$ high-entropy alloys on aluminum. *Mater Res Express.* 2020;7(8):086504.
- Duarte T, Meyer YA, Osório WR. The holes of Zn phosphate and hot dip galvanizing on electrochemical behaviors of multi-coatings on steel substrates. *Metals.* 2022;12(5):863.
- Meyer YA, Bonatti RS, Bortolozzo AD, Osório WR. Electrochemical behavior and compressive strength of Al-Cu/xCu composites in NaCl solution. *J Solid State Electrochem.* 2021;25(4):1303-17.
- Zhang XL, Jiang ZH, Yao ZP, Song Y, Wu ZD. Effects of scan rate on the potentiodynamic polarization curve obtained to determine the Tafel slopes and corrosion current density. *Corros Sci.* 2009;51(3):581-7.
- McCafferty E. Validation of corrosion rates measured by the Tafel extrapolation method. *Corros Sci.* 2005;47(12):3202-15.
- Zhou Y, Yan F. Electrochemical micro-couple mechanism based on Si and Mn segregations revealing the initiation of grain boundary dissolution for Q235 carbon steel. *J Ind Eng Chem.* 2023;120:131-9.
- Wang X, Li G, He Q, Jiang J, Li D, Shao W, et al. Intergranular corrosion of an Al-Cu-Li alloy: the influence from grain structure. *Corros Sci.* 2023;211:110845.
- Verissimo NC, Freitas ES, Cheung N, Garcia A, Osório WR. The effects of Zn segregation and microstructure length scale on the corrosion behavior of a directionally solidified Mg-25 wt.%Zn alloy. *J Alloys Compd.* 2017;723:649-60.
- Vida TA, Freitas ES, Cheung N, Garcia A, Osório WR. Electrochemical corrosion behavior of as-cast Zn-rich Zn-Mg alloys in a 0.06M NaCl solution. *Int J Electrochem Sci.* 2017;12(6):5264-83.
- Hirschorn B, Orazem ME, Tribollet B, Vivier V, Frateur I, Musiani M. Determination of effective capacitance and film thickness from constant-phase-element parameters. *Electrochim Acta.* 2010;55(21):6218-27.
- Hirschorn B, Orazem ME, Tribollet B, Vivier V, Frateur I, Musiani M. Constant-phase-element behavior caused by resistivity distributions in films II. Applications. *J Electrochem Soc.* 2010;157(12):C458-63.
- Ferraa S, Ouakki M, Barebita H, Nimour A, Cherkaoui M, Guedira T. Corrosion inhibition potentials of some phosphovanadate-based glasses on mild steel in 1 M HCl. *Inorg Chem Commun.* 2021;132:108806.
- Shon Y, Joshi SS, Katakam S, Shanker Rajamure R, Dahotre NB. Laser additive synthesis of high entropy alloy coating on aluminum: corrosion behavior. *Mater Lett.* 2015;142:122-5.